Lawrence Berkeley National Laboratory
Recent Work

Title
Buried Interfaces in Halide Perovskite Photovoltaics.

Permalink

Journal
Advanced materials (Deerfield Beach, Fla.), 33(7)

Authors
Yang, Xiaoyu
Luo, Deying
Xiang, Yuren
et al.

Publication Date
2021-02-01

Peer reviewed

Buried Interfaces in Halide Perovskite Photovoltaics

Xiaoyu Yang, Deying Luo, Yuren Xiang, Lichen Zhao, Miguel Anaya, Yonglong Shen, Jiang Wu, Wenqiang Yang, Yu-Hsien Chiang, Yongguang Tu, Rui Su, Qin Hu, Hongyu Yu, Guosheng Shao, Wei Huang, Thomas P. Russell, Qihuang Gong,* Samuel D. Stranks, Wei Zhang,* and Rui Zhu*

ABSTRACT: Understanding the fundamental properties of buried interfaces in perovskite photovoltaics is of paramount importance to the enhancement of device effi-ciency and stability. Nevertheless, accessing buried interfaces poses a sizeable challenge because of their non-exposed feature. Herein, the mystery of the buried interface in full device stacks is deciphered by combining advanced in situ spectroscopy techniques with a facile lift-off strategy. By establishing the microstructure–property relations, the basic losses at the contact interfaces are systematically presented, and it is found that the buried interface losses induced by both the sub-microscale extended imperfections and lead-halide inhomo-geneities are major roadblocks toward improvement of device performance. The losses can be considerably mitigated by the use of a passivation-molecule-assisted microstructural reconstruction, which unlocks the full potential for improving device performance. The findings open a new avenue to under-standing performance losses and thus the design of new passivation strategies to remove imperfections at the top surfaces and buried interfaces of perovskite photovoltaics, resulting in substantial enhancement in device performance.

Halide perovskite photovoltaics have gained enormous attention because of their ever-increasing power conversion efficiencies (PCEs) over the past few years.[1–6] Further improvements in the performance of perovskite photovoltaics are hampered by a lack of in-depth under-standing of the heterojunction interfaces and optimal interface designs,[7–9] specifi-cally the buried interfaces within polycrys-talline perovskite films.[10–14] Studies to date have focused on the top surfaces,[15–17] yet undesirable non-radiative losses that hinder the device power outputs are known to exist at the interfaces with bottom contact layers due to the accumu-lation of deep-level trap states.[12,18] For example, though empirical device optimi-zation approaches suggest that the excess lead halide in the perovskite starting

X. Yang, Dr. D. Luo, Dr. L. Zhao, Dr. J. Wu, Dr. W. Yang, R. Su,
Prof. Q. Gong, Prof. R. Zhu
State Key Laboratory for Artificial Microstructure and Mesoscopic Physics
School of Physics
Frontiers Science Center for Nano-optoelectronics, and Collaborative
Innovation Center of Quantum Matter
Peking University
Beijing 100871, China
E-mail: qhgong@pku.edu.cn; iamzhurui@pku.edu.cn

Dr. D. Luo, Prof. H. Yu
School of Microelectronics
Southern University of Science and Technology
Shenzhen 518055, China

Dr. Y. Xiang, Prof. W. Zhang
Advanced Technology Institute
University of Surrey
Guildford GU2 7XH, UK
E-mail: wz0003@surrey.ac.uk

Dr. M. Anaya, Y.-H. Chiang, Prof. S. D. Stranks
Cavendish Laboratory
University of Cambridge
Cambridge CB3 0HE, UK

Dr. Y. Shen, Prof. G. Shao
State Centre for International Cooperation on Designer
Low-Carbon and Environmental Material (SCICDLCEM)
School of Materials Science and Engineering
Zhengzhou University
Zhengzhou 450001, China

Dr. W. Yang, Dr. Q. Hu, Prof. T. P. Russell
Materials Sciences Division
Lawrence Berkeley National Laboratory
Berkeley, CA 94720, USA

Prof. Y. Tu, Prof. W. Huang
Frontiers Science Center for Flexible Electronics
Xi'an Institute of Flexible Electronics (IFE)
Northwestern Polytechnical University
Xi'an 710072, China

Dr. Q. Hu, Prof. T. P. Russell
Department of Polymer Science and Engineering
University of Massachusetts
Amherst, MA 01003, USA

Prof. Q. Gong, Prof. R. Zhu
Collaborative Innovation Center of Extreme Optics
Shanxi University
Taiyuan, Shanxi 030006, China

Prof. Q. Gong, Prof. R. Zhu
Peking University Yangtze Delta Institute of Optoelectronics
Nantong, Jiangsu 226010, China

Prof. S. D. Stranks
Department of Chemical Engineering and Biotechnology
University of Cambridge
Cambridge CB3 0AS, UK

The ORCID identification number(s) for the author(s) of this article
can be found under https://doi.org/10.1002/adma.202006435.

solution has a beneficial effect of bulk crystallization and passivation,[19,20] the large amounts of excess lead halide existing at the buried interface could vary the surface electronic states and behave like traps. Consequently, it is urgently needed to compromise between these detrimental effects and beneficial effects. However, exploring these issues will become complex when the excess lead halide accumulates at the buried interface featuring non-exposed characteristics. Although in situ techniques have been developed to study buried interfaces in full devices,[21,22] directly visualizing buried microstructures along with their local semiconductor nature has never been realized. It is yet rather pressing to find ways to access the buried interfaces to achieve device efficiency limits.[23]

We present a simple and effective lift-off process to expose and uncover the buried interfaces of pristine and robust polycrystalline perovskite films. By combining interface and surface characterizations, we show that the losses at buried interfaces arise from the sub-microscale imperfections and inhomogeneities. Both of these are introduced by the complex phases comprising multiple nanoscale lead-halide crystallites, and even just tiny excess ends up being detrimental at the interfaces. By exploiting time-related confocal spectroscopic imaging and materials characterizations, we also demonstrate that the substantial sub-micrometer imperfections and heterogeneities can be mitigated at both top surfaces and buried interfaces through a passivation-molecule-assisted microstructural reconstruction.

To generate the state-of-the-art polycrystalline perovskites used for experimental observations, we begin with one of the most commonly used mixed-cation lead mixed-halide perovskites for perovskite solar cells (PSCs),[24,25] $FA_{0.81}MA_{0.10}Cs_{0.04}PbI_{2.55}Br_{0.40}$ (FA and MA are formamidinium and methylammonium, respectively) (Figure S1 and Table S1, Supporting Information). The outstanding photovoltaic performances of PSCs from these materials confirm the high quality of the pristine film used throughout this work. Without passivation (control devices), inverted PSCs consisting of indium tin oxide (ITO)/poly[bis (4-phenyl) (2,4,6-trimethylphenyl)amine] (PTAA)/perovskite/[6,6]-phenyl-C_{61}-butyric acid methyl ester (PC$_{61}$BM)/buckminsterfullerene (C_{60})/bathocuproine (BCP)/Cu deliver PCEs of up to 19.92%. By contrast, regular PSCs comprising ITO/SnO$_2$/perovskite/2,2′,7,7′-tetrakis(N,N-dipmethoxyphenylamine)-9, 9′-spirobifluorene (Spiro-OMeTAD)/Au show PCEs of 20.67%. Upon an ammonium-halide post-treatment passivation with n-hexyltrimethyl ammonium bromide (n-HABr), the PCEs increase to 22.26% and 23.11% for the inverted and regular PSCs, respectively, and both exhibit comparable stabilized power outputs tracked at the maximum power points.

The lift-off process is schematized in **Figure 1**a and shown in Video S1, Supporting Information. We first validate that the lift-off process does not alter the structure, morphology, and optical features of polycrystalline perovskite films (see Figure S2 and Note S1, Supporting Information, for details), enabling in-depth characterizations of the previously inaccessible buried interfaces and the potential impacts of the passivation. Firstly, cross-sectional techniques enable direct observations of the microstructures of the perovskite films in inverted PSCs. From the scanning electron microscopy (SEM) image of the control device (Figure 1b), the perovskite grains closely pack normal to the interface. Bright grains are distributed throughout the

perovskite thin film, while some small grains are located near the top interface and other flaky grains are located at the grain boundaries near the buried interface. Transmission electron microscopy (TEM) is used to determine their compositions and crystal structures (Figure 1c and Figure S3, Supporting Information). The high-angle annular dark-field scanning transmission electron microscopy (HAADF-STEM) image and corresponding energy disperse X-ray (EDX) elemental mappings confirm that the brighter strip-like structures are the large bright flaky grains observed by SEM, which predominately consist of lead (Pb), iodine (I), and bromide (Br), with the larger average atomic number evident from backscattered electrons (even when the detector is pulled away from the standard detector position in the second electron imaging mode). The large strip-like grains show highly oriented lattice lines (in the selected area denoted as "1") corresponding to the crystal planes of the hexagonal lead mixed-halide crystals, determined by indexing the diffraction spots in the selected area (denoted as "2"), with a lattice spacing of 6.66 Å, closely matching the PbI$_2$ (005) crystal plane (6.98 Å, PDF No. 73–1286). Such electron diffraction patterns are different from those of the perovskite crystals near the strip-like grains (Figure S3b, Supporting Information). From the X-ray diffraction (XRD) patterns of the perovskite film (Figure S2b, Supporting Information), we note that the diffraction peak at ≈13.1° is larger than that of the PbI$_2$ (≈12.7°), in agreement with a smaller lattice spacing for the strip-like grains obtained by TEM. When I ions (radius 1.70 Å) are substituted by Br ions (radius 1.06 Å), the lattice spacing of the PbI$_2$ crystal will decrease due to the smaller radius of Br ions, since the strip-like grains have a composition of PbI$_{2-x}$Br$_x$. Through further analysis of the crystalline features near the strip-like grains, we note that there are randomly distributed smaller lead-halide grains near the strip-like PbI$_{2-x}$Br$_x$, forming the sub-microscale complex phases comprising multiple nanoscale lead halides and adjacent perovskites surrounding those lead halides (Figure S3c, Supporting Information).

To compare the differences between the top and bottom sides of the polycrystalline film, we used the lift-off technique to expose the buried interface of the perovskite film. From the SEM images for both sides of the perovskite film, the larger perovskite grain sizes (≈233 ± 8 nm) are observed on the bottom side, in comparison to those on the top side (≈186 ± 6 nm, **Figure 2**a,b and Figure S4a, Supporting Information). Moreover, the bottom side presents large flaky lead-halide grains aligned almost normal to the substrate, consistent with the cross-sectional SEM and TEM results. By contrast, the top side is more uniform, with smaller lead-halide grains filling in the perovskite grain boundaries. We also note that the accumulation of large flaky lead halides at the bottom side is commonly observed in a variety of perovskites processed from the PbI$_2$-excess precursor, regardless of the bottom contacts on which the perovskites are crystallized (Figure S4c,d, Supporting Information). For the stoichiometric perovskite film (made from the precursor without excess PbI$_2$), the bottom side is less compact in comparison to those processed from the precursor with excess PbI$_2$ (Figure S4b, Supporting Information), which is likely due to different film growth processes.[22]

To characterize the chemical composition distribution of both sides, we performed nanoscale-resolved Fourier transform infrared (nano-FTIR) microscopy and X-ray
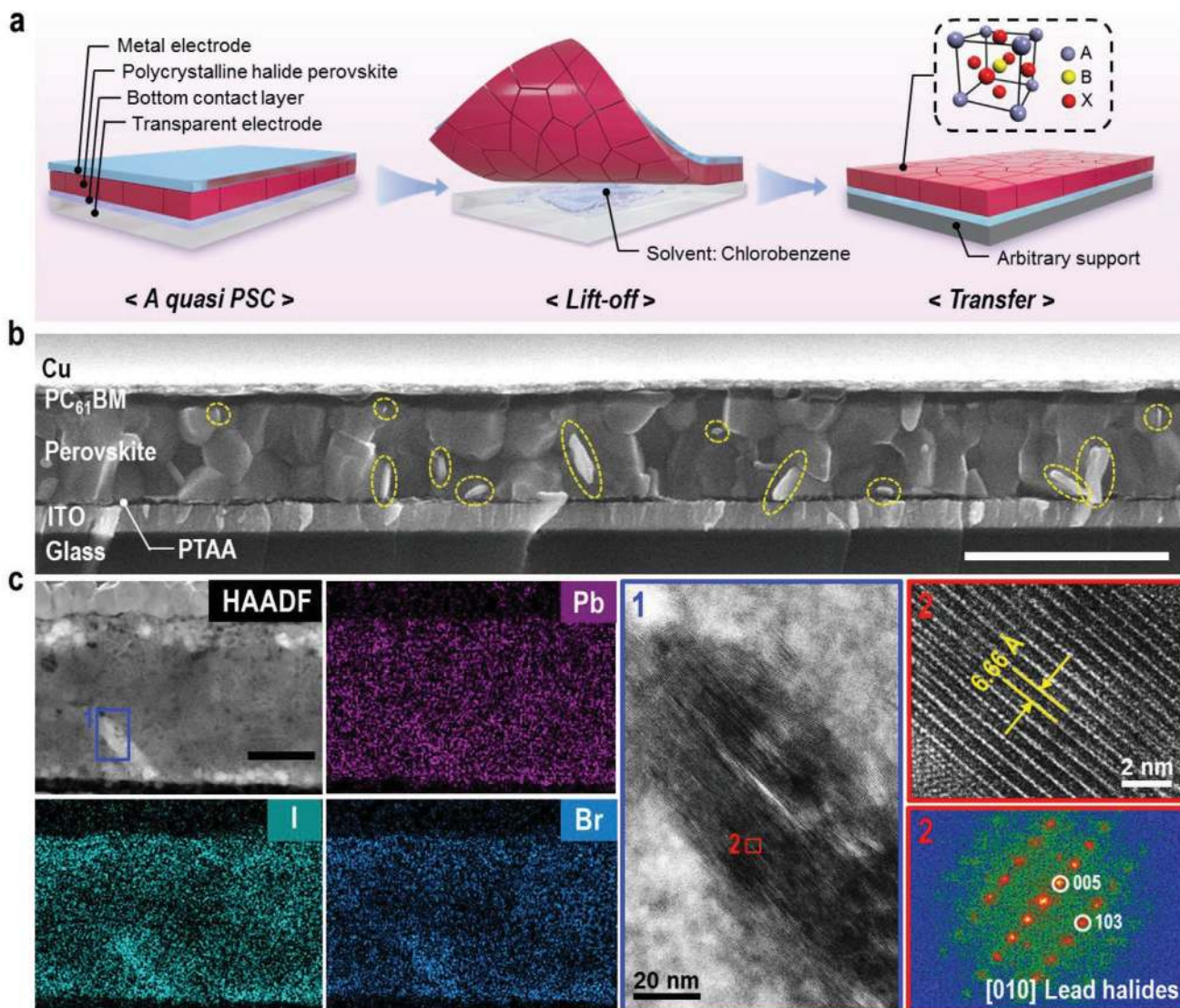
Figure 1. a) Schematic of the lift-off process. A: monovalent organic or inorganic cations, B: Pb^{2+}, X: halogen anions. b) Cross-sectional SEM image of inverted PSCs. The bright grains are highlighted by the yellow dotted circles or ellipses. Scale bar: 2 μm. c) The sectional HAADF-STEM and corresponding EDX images from the quasi-PSC, highlighting the brighter contrast in the HAADF image owing to the larger average atomic number. Selected area 1: The enlarged TEM image of the flaky crystal near the buried interface. Selected area 2: The high-resolution lattice image and corresponding fast Fourier transform (FFT) pattern of the flaky crystal. Scale bar in the HAADF image: 200 nm.

photoelectron spectroscopy (XPS). The non-destructive chemical mapping afforded by nano-FTIR allows us to resolve the spatial distribution of the organic components near the surfaces of the film (≈10 nm). From the nano-FTIR white-light imaging (Figure 2c,d and Figure S5a, Supporting Information), we observe more pronounced inhomogeneity for the lateral concentration of the dominant A-site cation (FA$^+$; the MA$^+$ is below the detection level) at the bottom side in comparison to the top side (Figure 2e). This could arise from the local accumulation of organic components or the existence of flaky lead halides at the bottom side during annealing/cooling.[26] XPS characterization shows that the average ([I] + [Br])/[Pb] ratios are 2.81 and 2.32 for the top side and bottom side, respectively, with respect to the nominal value of 2.95 (Figure S5b, Supporting Information),

further emphasizing the uneven chemical distributions on both sides. Moreover, we also observe that the signals from metallic Pb (Pb^0) are absent in the XPS spectra (Pb 4f) of the bottom side but are evident on the surface (top side) of the perovskite film as reported elsewhere,[27] although the origin of the Pb^0 remains elusive.

To probe the local energetic variation, Kelvin probe force microscopy (KPFM) was used to correlate the surface potential with topography. We note that the flaky lead halides at the bottom side have larger surface potentials (≈50 mV) with respect to the rest of the film, significantly changing the local distribution of the bottom energy levels (Figure 2f). While on the top side, the surface potentials are more homogeneous (Figure S5c, Supporting Information) than those of the bottom. Consequently, the morphologies and surface
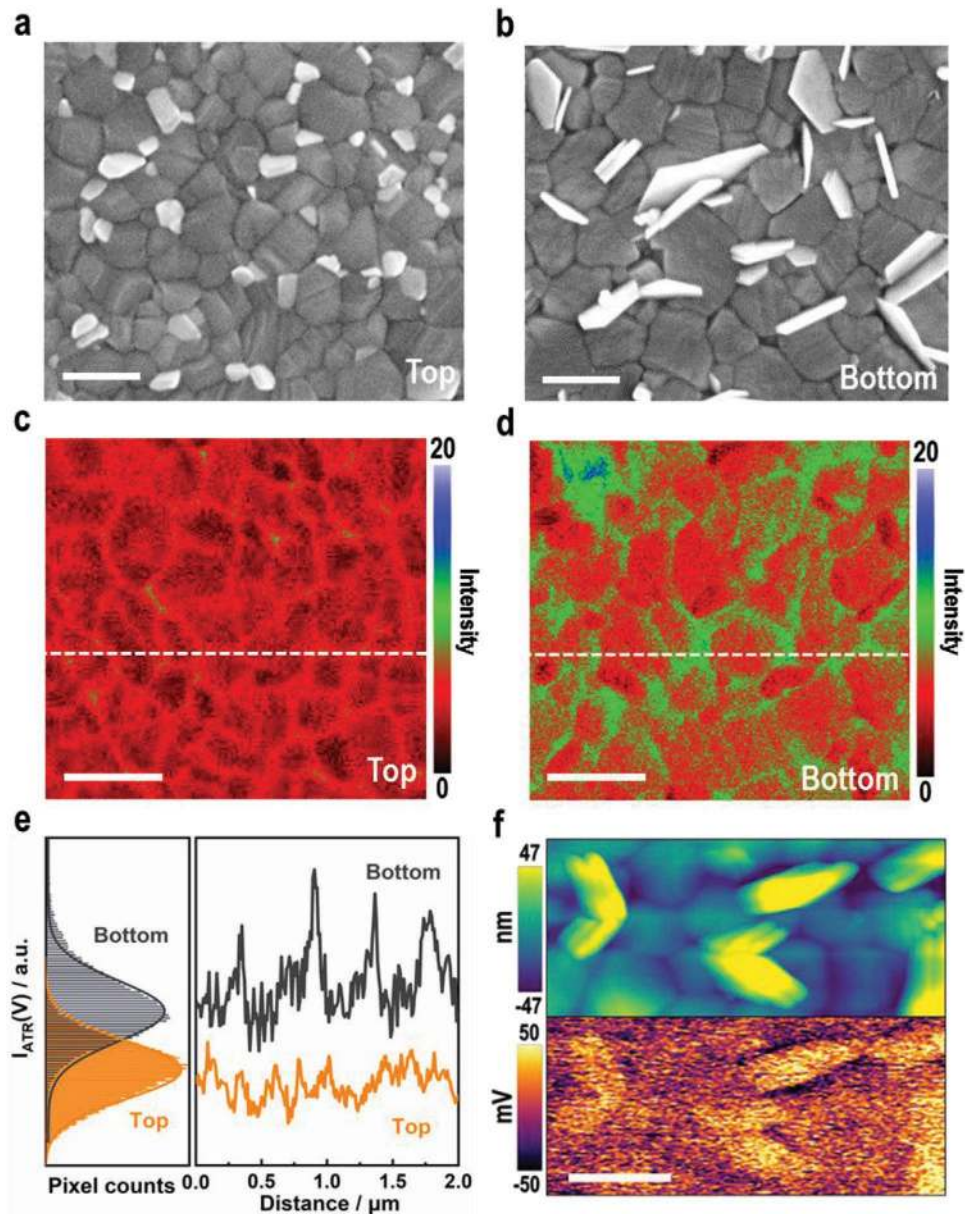
Figure 2. a,b) SEM images of the top (a) and bottom (b) sides of the perovskite films. c,d) FA$^+$ spatial distribution of the top (c) and bottom (d) sides obtained from nano-FTIR over the wavenumber range of 1500–1900 cm^{-1}. Color bar: the normalized intensity of the reflection signals from the sample. e) The statistical distribution of infrared radiation (IR) intensities of both sides, and the collected IR intensities from the white dotted lines in (c) and (d). f) AFM image (top panel), and corresponding KPFM image (bottom panel) of the bottom side. Scale bars for all figures: 0.5 μm.

potentials are distinct for both sides, probably owing to the heterogeneous morphological and chemical distribution as discussed above.[28]

To correlate the optoelectronic properties with the observed features at the microscale, we performed confocal photoluminescence (PL) imaging on the top and exposed bottom sides. A 470-nm pulsed laser illumination was employed to generate excitations near the surface of the film (1/e excitation depth of ≈70 nm). The detection wavelength ranges were set to 700–790 nm to identify the perovskites and 500–570 nm to monitor the emission from the lead halides that exhibit a PL peak centered at ≈506 nm (Figure S6a,

Supporting Information). From the PL mapping of the top side, we observe relatively spatial homogeneous PL signals from the perovskite grains, with weak signals arising from the lead halides surrounding perovskite grains (**Figure 3**a). By contrast, the bottom side is more inhomogenous, exhibiting a high density of regions with low-luminous perovskite grains and sub-microscale dark regions (Figure 3b). Note that in most dark regions, the flaky lead-halide emissions are detected even if both are not perfectly overlapping. The perovskite PL intensity is found to decrease with the appearance of the lead-halide signals, which confirms the grain-to-boundary PL heterogeneities at the bottom side (Figure 3c). The carrier
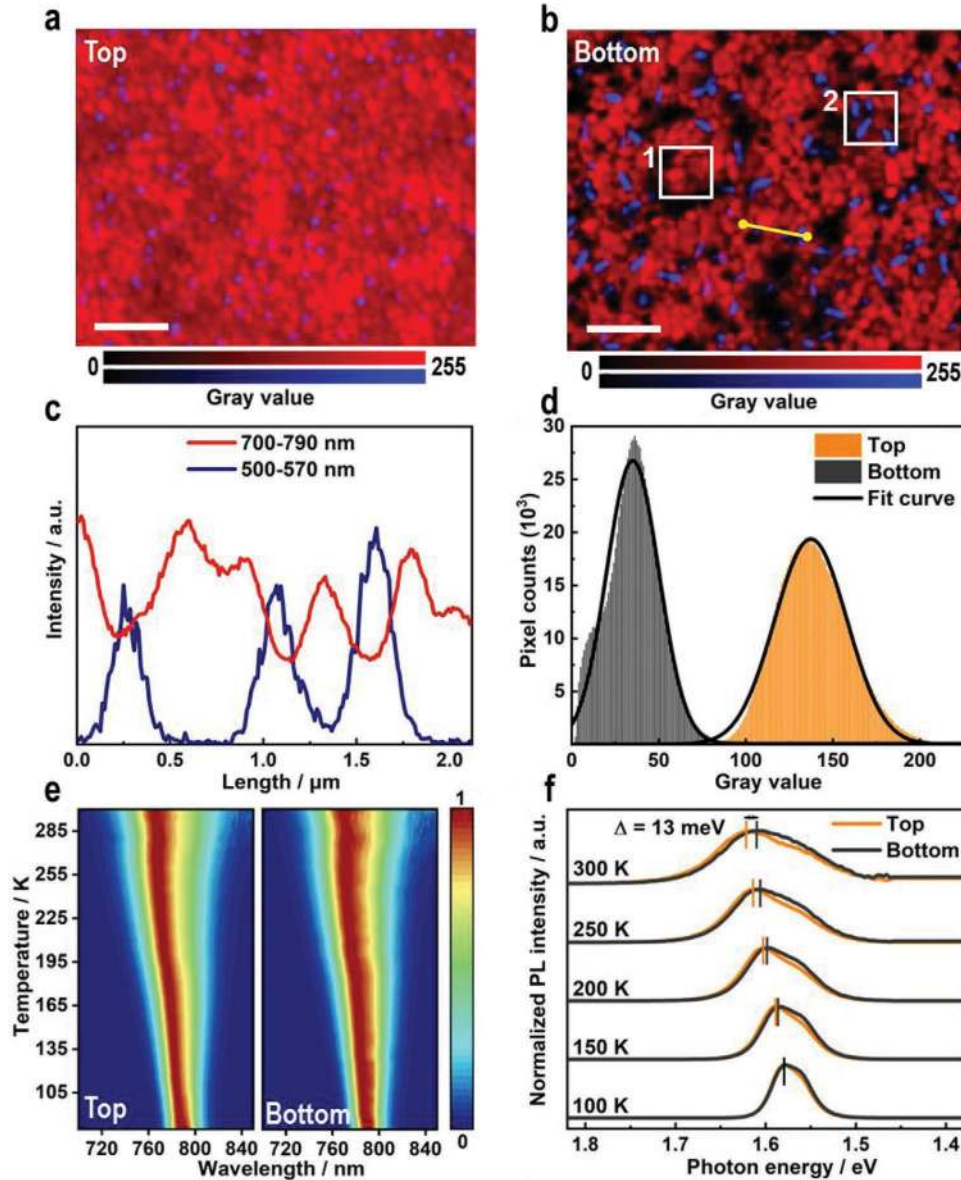
Figure 3. a,b) Confocal PL mapping images of the top (a) and bottom (b) sides. Scale bar: 2 μm. The ranges of the detection are 700–790 nm (red bar) and 500–570 nm (blue bar), respectively. c) The line scan of the PL intensities obtained from the yellow line in (b). d) The statistical distribution of the top and bottom PL grey values (0–255) extracted from the confocal PL mapping images. e) 2D temperature-dependent PL spectra taken from 80 to 300 K for both top and bottom sides from one perovskite film. f) The PL curves at different temperatures extracted from the 2D temperature-dependent PL spectra.

lifetimes extracted from two regions selected on the bottom side (denoted as "1" and "2", where the selected regions 1 and 2 are dominated by pure perovskites and mixed perovskites/ lead halides, respectively) show more rapid recombination kinetics in region 2, indicating that the lead halides could accelerate the annihilation of the photo-generated charge carriers (Figure S6b, Supporting Information). Moreover, the histogram of PL intensities (from perovskites) represented by pixel counts indicates that the top side emits more photons than the bottom side under the same excitation conditions (Figure 3d), showing inferior PL properties at the bottom side of a polycrystalline perovskite film.

We observe the same effects on the buried interfaces of as-fabricated perovskite films, using a dedicated sample structure with an ultrathin transparent substrate (Figure S7a, Supporting Information). The consistent luminescence features, including sub-microscale dark regions along with the lead halides, are similar to those of the lift-off perovskite films (Figure S7b–e, Supporting Information). These sub-microscale dark regions negatively affect the excited-state charge-carrier population at the buried interface, as further evidenced by the reduced lifetime and external photoluminescence quantum efficiency (PLQE) when selectively exciting the buried interface of the as-fabricated samples compared to the top interface with

an excitation wavelength 550 nm that is below the absorption threshold of the lead halides (Figure S6c, Supporting Information). This means that the presence of these dark PL regions at the buried interface leads to device efficiency losses through non-radiative recombination.[29,30]

To gain a deeper insight into the inferior PL properties of the perovskite bottom side, we measured the temperature-dependent PL spectra for both sides (Figure 3e). As the peaks redshift with decreasing temperatures, the spectral peak widths become narrower. Even though both sides have similar PL spectra at low temperatures, they show a distinct evolution with increasing temperature, and finally the PL peak of the bottom side redshifts by 13 meV with respect to its top-side counterpart at 300 K (Figure 3f). This behavior arises from the difference in the band structures, which may originate from the inconsistently chemical compositions on both sides as verified by nano-FTIR and XPS measurements. Moreover, the full width at half maximum (FWHM) of the PL peak can be broadened by the scattering processes between charge carriers and phonons or impurities.[31] We further calculate the electron–phonon coupling (Γ_{op}) for both sides by fitting the temperature-dependent FWHM over the range 80–300 K (Figure S6d and Table S3, Supporting Information). The Γ_{op} of the bottom side ($\Gamma_{op,bottom} \approx 167.5$ meV) is estimated to be greater than that of the top side ($\Gamma_{op,top} \approx 77.2$ meV), confirming the inferior crystal qualities and PL properties at the bottom side. We also associate the larger estimated inhomogeneous broadening term (Γ_0) of the bottom side with imperfections and serious structural disorder stemming from variations of local compositions and structures.[28] These results collectively show that the multi-scale heterogeneities and imperfections permeate the perovskite film, particularly at the buried interface, and ultimately result in different optoelectronic behaviors on both sides of a polycrystalline perovskite film.

In order to assess whether we can regulate these imperfections and multi-scale heterogeneities of buried interfaces and link these changes to the device performance, we use the n-HABr as a post-treatment passivation molecule since the n-HABr shows the most outstanding capabilities in the efficiency improvements and has a largest cation size in a variety of the passivation molecules.[2,16,32,33] In practice, we first spin-coated a layer of the n-HABr on the top of the as-prepared perovskite film that is processed by regular routes and subsequently monitor the local changes of the lead halides and the sub-microscale dark regions at the buried interfaces by confocal PL maps at a different annealing time of 100 °C (**Figure 4**). Initially, we see the distribution of both lead halides and the dark regions, but over the first 1 min of annealing, most of the lead halides are eliminated while the sub-microscale dark regions remain stable. After 10 min of annealing, both the lead-halide signals and sub-microscale dark regions disappear while both the PL intensity and spatial homogeneity of the perovskite substantially improves. These improvements are also confirmed in very spatially uniform and luminescent-enhanced PL mappings on the bottom side of the lift-off perovskites (Figure S7f, Supporting Information).

To demonstrate the improvements in the confocal PL mappings at buried interfaces of the passivated films, we show the variation of the morphologies of both sides of a perovskite film after the ammonium-halide passivation (**Figure 5**a,b). Notably,

the passivated perovskite film exhibits a lead-halide elimination microstructural reconstruction in comparison to the control film (Figure 2a,b). Moreover, we also observe similar changes in the microstructure of the perovskite films treated by a series of other ammonium-halide molecules (with different molecular sizes) which are broadly utilized in the best-performing PSCs[2,16,32,33] (Figure S8, Supporting Information). Upon lead-halide elimination microstructural reconstruction, the ratios of both [Br]/[Pb] and ([I] + [Br])/[Pb] on the bottom side increase and are close to the nominal values as confirmed by XPS (Figure S9a, Supporting Information), suggesting a reduction of local non-stoichiometric components. The absence of lead halides in the passivated perovskite films also results in more uniform surface-potential mapping by KPFM (Figure S9b, Supporting Information). These improvements have a positive impact on enhancing the PLQE value of the passivated film as compared to the control: the bottom side increasing from (1.92 ± 0.55)% to (15.18 ± 0.45)%, from (2.41 ± 0.31)% to (14.95 ± 0.68)% for the top side (Figure 5e). Thus, the microstructural reconstruction through the ammonium-halide passivation plays a key role in improving optoelectronic properties over the entire film.

To probe the variation of the crystallographic structures and to clarify what happens upon microstructural reconstruction, the grazing-incidence wide-angle X-ray scattering (GIWAXS) technique is used to obtain the crystallographic information of the perovskite film at different penetration depths. Figure 4c,d compares 2D GIWAXS patterns for the top and bottom sides of the ammonium-halide-passivated perovskite film with an incidence angle of 0.3°, respectively (patterns for the incidence angles of 0.1° and 0.5° and the GIWAXS information of control sample are provided in Figure S10a,b, Supporting Information). The integrated signals of the reflections located at ≈0.39, ≈0.46, and ≈0.67 Å^{-1} in Figure 4f at different incidence angles on both sides of the film are used to track the ammonium-halide–perovskite complex and confirm its permeation through the film.[15] With increasing penetration depth from the bottom side, the reflections at ≈0.46 and ≈0.67 Å^{-1} gradually increase, while that at ≈0.39 Å^{-1} decreases. It suggests that the preferential orientation of the ammonium-halide–perovskite complex varies remarkably at the bottom side, due more likely to the physical constraint at the interface of the perovskite/bottom contact layer. In addition, a series of enhanced signals at ≈0.58 Å^{-1} of perovskites (as shown in Figure S10b, Supporting Information) at the bottom side could be associated with the ammonium-halide-induced reconstructions of perovskites. We further investigate the quality of the bottom side through the microstrain. Based on the Williamson–Hall analysis of the integrated GIWAXS signals, the estimated microstrain near the bottom side of the ammonium-halide-passivated films decreases from (1.39 ± 0.02)% for the control to (1.17 ± 0.04)% (Figure 5g, and see Note S5, Supporting Information, for details). This reduced microstrain and overall improved properties for the ammonium-halide-passivated samples suggest that, even though the cation size of the n-HABr (≈8.9 Å) and other similar molecules are larger than the FA cation (≈2.6 Å), the imperfection of the buried interface can be improved by the molecule-passivation-assisted microstructural reconstruction, in the right direction to substantial improvements in the entire film quality (including both top and buried interfaces).
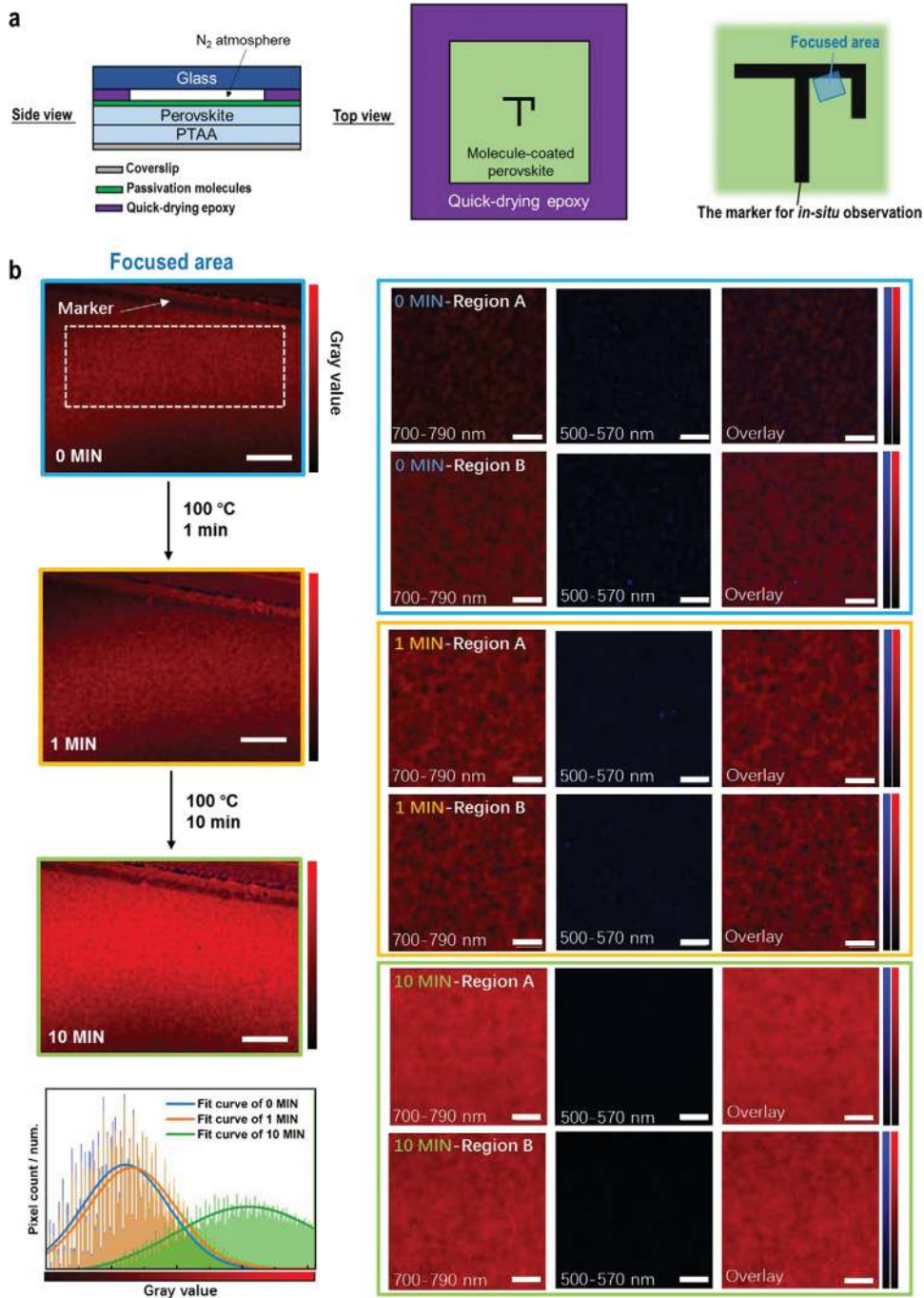
Figure 4. a) The side and top views of the dedicated sample configuration, and the marker for the time-correlated observation. b) The confocal PL mappings of the focused areas and the gray-value distribution of the white dashed area at the buried interface from 0 to 10 min. Time-correlated PL mapping evolution of two randomly selected regions (named Region A and B) in the white dashed rectangle at different annealing time. Scale bars: 20 μm for focused area, 2 μm for the randomly selected regions.

By analyzing the fundamental properties of the buried interface of the pristine films including morphology, chemical composition, electronic structure, and photophysics, we find that the sub-microscale imperfections and inhomogeneities accumulating at the buried interfaces limit devices from reaching their performance potentials. We show that those imperfections and inhomogenities arise from a wide variety of complex phases. The complex phases consist of various nanoscale lead-halide crystallites at the buried interface that are directly related to undesirable non-radiative recombination centers, although empirical device optimization shows that a small fraction of excess lead-halide in the starting precursor solution benefits the film crystallization.[20] Both are sensitive to the excess lead-halide fraction, and optimally
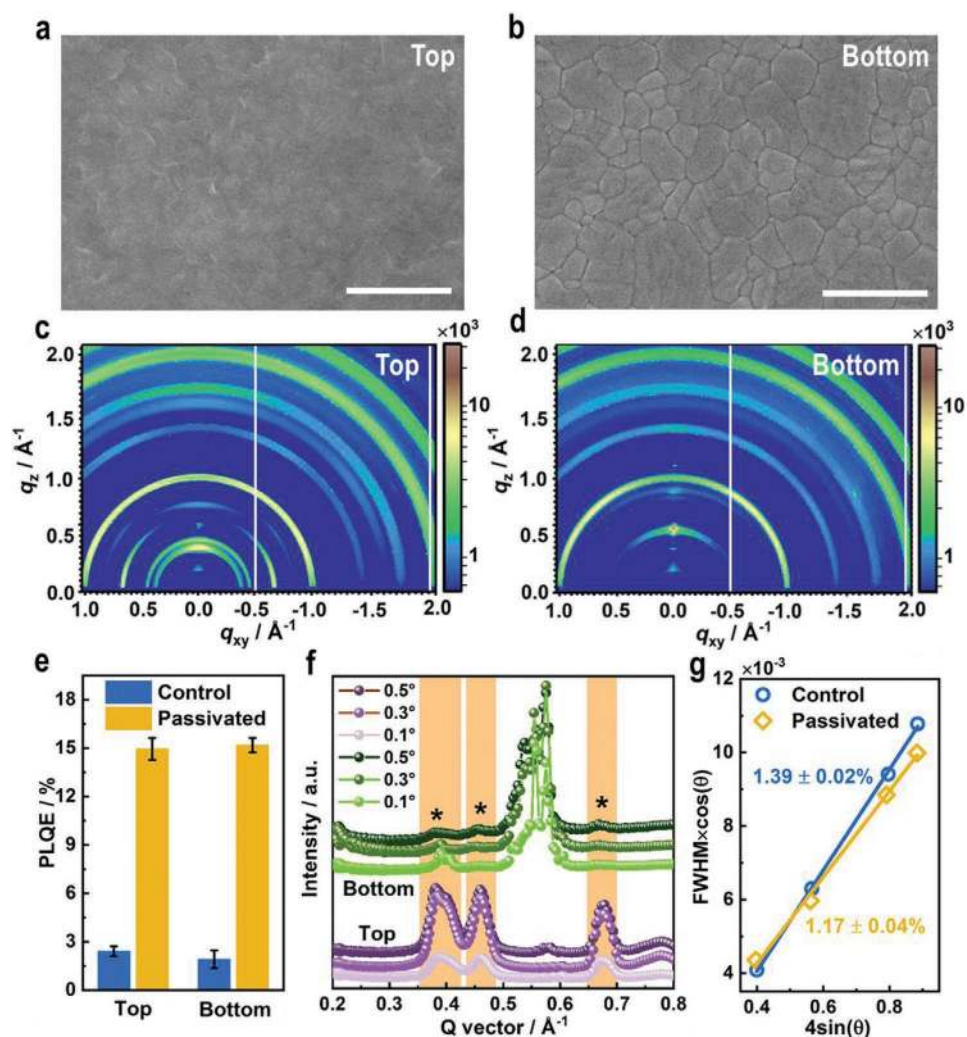
Figure 5. a,b) The morphologies for both top (a) and bottom (b) sides of the ammonium-halide-passivated perovskite films. Scale bar: 1 μm. c,d) GIWAXS 2D patterns for both top (c) and bottom (d) sides of the passivated sample at the beam incidence angle of 0.3°. e) The PLQE results for the bottom sides of the perovskite films with and without ammonium-halide passivation. f) The integrated signals for both sides at different incidence angles in the Q vector range of 0.2–0.8 Å^{-1} (* denotes the ammonium-halide–perovskite complex). g) The microstrain analysis for the bottom sides of the perovskite films with and without ammonium-halide passivation.

balancing these two counteracting effects is extremely difficult to achieve in practice. Passivation approaches including the use of ammonium halides will be essential to mitigate these undesirable imperfections by varying the morphology and crystallographic structure by a molecule-assisted microstructural reconstruction. This improvement is associated with the diffusion of the passivation molecules during the post-annealing process. We reckon that advanced microscopy techniques coupled with high spatial resolution imaging will help to elucidate the structure–function relationship at buried interfaces of individual grains, and ultimately an in-depth understanding of polycrystalline perovskite thin films. Hence, the methodology reported in this work represents a starting point to uncover the properties of the buried interfaces of various perovskite compositions and device structures for a broad range of applications including PSCs, light-emitting diodes, photodetectors, and other perovskite optoelectronics.

Supporting Information

Supporting Information is available from the Wiley Online Library or from the author.

Acknowledgements

Conflict of Interest

The authors declare no conflict of interest.

Keywords

buried interfaces, imperfections, microstructural reconstruction, perovskite photovoltaics

[1] H. Min, M. Kim, S.-U. Lee, H. Kim, G. Kim, K. Choi, J. H. Lee, S. I. Seok, *Science* **2019**, *366*, 749.

[2] D. Luo, W. Yang, Z. Wang, A. Sadhanala, Q. Hu, R. Su, R. Shivanna, G. F. Trindade, J. F. Watts, Z. Xu, T. Liu, K. Chen, F. Ye, P. Wu, L. Zhao, J. Wu, Y. Tu, Y. Zhang, X. Yang, W. Zhang, R. H. Friend, Q. Gong, H. J. Snaith, R. Zhu, *Science* **2018**, *360*, 1442.

[3] X. Zheng, Y. Hou, C. Bao, J. Yin, F. Yuan, Z. Huang, K. Song, J. Liu, J. Troughton, N. Gasparini, C. Zhou, Y. Lin, D.-J. Xue, B. Chen, A. K. Johnston, N. Wei, M. N. Hedhili, M. Wei, A. Y. Alsalloum, P. Maity, B. Turedi, C. Yang, D. Baran, T. D. Anthopoulos, Y. Han, Z.-H. Lu, O. F. Mohammed, F. Gao, E. H. Sargent, O. M. Bakr, *Nat. Energy* **2020**, *5*, 131.

[4] Y. Tu, G. Xu, X. Yang, Y. Zhang, Z. Li, R. Su, D. Luo, W. Yang, Y. Miao, R. Cai, L. Jiang, X. Du, Y. Yang, Q. Liu, Y. Gao, S. Zhao, W. Huang, Q. Gong, R. Zhu, *Sci. China: Phys., Mech. Astron.* **2019**, *62*, 974221.

[5] M. Abdi-Jalebi, Z. Andaji-Garmaroudi, S. Cacovich, C. Stavrakas, B. Philippe, J. M. Richter, M. Alsari, E. P. Booker, E. M. Hutter, A. J. Pearson, S. Lilliu, T. J. Savenije, H. Rensmo, G. Divitini, C. Ducati, R. H. Friend, S. D. Stranks, *Nature* **2018**, *555*, 497.

[6] X. Yang, Y. Fu, R. Su, Y. Zheng, Y. Zhang, W. Yang, M. Yu, P. Chen, Y. Wang, J. Wu, D. Luo, Y. Tu, L. Zhao, Q. Gong, R. Zhu, *Adv. Mater.* **2020**, *32*, 2002585.

[7] Y. Yang, M. Yang, D. T. Moore, Y. Yan, E. M. Miller, K. Zhu, M. C. Beard, *Nat. Energy* **2017**, *2*, 16207.

[8] H. Tan, A. Jain, O. Voznyy, X. Lan, F. P. G. Arquer, J. Z. Fan, R. Quintero-Bermudez, M. Yuan, B. Zhang, Y. Zhao, F. Fan, P. Li, L. N. Quan, Y. Zhao, Z.-H. Lu, Z. Yang, S. Hoogland, E. H. Sargent, *Science* **2017**, *355*, 722.

[9] P. Schulz, D. Cahen, A. Kahn, *Chem. Rev.* **2019**, *119*, 3349.

[10] H. J. Snaith, S. Lilliu, *The Path to Perovskite on Silicon PV* **2018**, https://doi.org/10.32386/scivpro.000004.

[11] S. Bai, P. Da, C. Li, Z. Wang, Z. Yuan, F. Fu, M. Kawecki, X. Liu, N. Sakai, J. T.-W. Wang, S. Huettner, S. Buecheler, M. Fahlman, F. Gao, H. J. Snaith, *Nature* **2019**, *571*, 245.

[12] M. Stolterfoht, C. M. Wolff, J. A. Márquez, S. Zhang, C. J. Hages, D. Rothhardt, S. Albrecht, P. L. Burn, P. Meredith, T. Unold, D. Neher, *Nat. Energy* **2018**, *3*, 847.

[13] Y. Zheng, R. Su, Z. Xu, D. Luo, H. Dong, B. Jiao, Z. Wu, Q. Gong, R. Zhu, *Sci. Bull.* **2019**, *64*, 1255.

[14] S. P. Harvey, F. Zhang, A. Palmstrom, J. M. Luther, K. Zhu, J. J. Berry, *ACS Appl. Mater. Interfaces* **2019**, *11*, 30911.

[15] E. H. Jung, N. J. Jeon, E. Y. Park, C. S. Moon, T. J. Shin, T.-Y. Yang, J. H. Noh, J. Seo, *Nature* **2019**, *567*, 511.

[16] X. Zheng, B. Chen, J. Dai, Y. Fang, Y. Bai, Y. Lin, H. Wei, X. C. Zeng, J. Huang, *Nat. Energy* **2017**, *2*, 17102.

[17] J. J. Yoo, S. Wieghold, M. C. Sponseller, M. R. Chua, S. N. Bertram, N. T. P. Hartono, J. S. Tresback, E. C. Hansen, J.-P. Correa-Baena, V. Bulović, T. Buonassisi, S. S. Shin, M. G. Bawendi, *Energy Environ. Sci.* **2019**, *12*, 2192.

[18] Z. Ni, C. Bao, Y. Liu, Q. Jiang, W.-Q. Wu, S. Chen, X. Dai, B. Chen, B. Hartweg, Z. Yu, Z. Holman, J. Huang, *Science* **2020**, *367*, 1352.

[19] Y. C. Kim, N. J. Jeon, J. H. Noh, W. S. Yang, J. Seo, J. S. Yun, A. Ho-Baillie, S. Huang, M. A. Green, J. Seidel, T. K. Ahn, S. II Seok, *Adv. Energy Mater.* **2016**, *6*, 1502104.

[20] T. J. Jacobsson, J.-P. Correa-Baena, E. H. Anaraki, B. Philippe, S. D. Stranks, M. E. F. Bouduban, W. Tress, K. Schenk, J. Teuscher, J.-E. Moser, H. Rensmo, A. Hagfeldt, *J. Am. Chem. Soc.* **2016**, *138*, 10331.

[21] M. Xiao, T. Lu, T. Lin, J. S. Andre, Z. Chen, *Adv. Energy Mater.* **2020**, *10*, 1903053.

[22] M. Xiao, S. Joglekar, X. Zhang, J. Jasensky, J. Ma, Q. Cui, L. J. Guo, Z. Chen, *J. Am. Chem. Soc.* **2017**, *139*, 3378.

[23] D. Luo, R. Su, W. Zhang, Q. Gong, R. Zhu, *Nat. Rev. Mater.* **2020**, *5*, 44.

[24] M. Saliba, T. Matsui, J.-Y. Seo, K. Domanski, J.-P. Correa-Baena, M. K. Nazeeruddin, S. M. Zakeeruddin, W. Tress, A. Abate, A. Hagfeldt, M. Grätzel, *Energy Environ. Sci.* **2016**, *9*, 1989.

[25] N. Arora, M. I. Dar, A. Hinderhofer, N. Pellet, F. Schreiber, S. M. Zakeeruddin, M. Grätzel, *Science* **2017**, *358*, 768.

[26] C. Zhu, X. Niu, Y. Fu, N. Li, C. Hu, Y. Chen, X. He, G. Na, P. Liu, H. Zai, Y. Ge, Y. Lu, X. Ke, Y. Bai, S. Yang, P. Chen, Y. Li, M. Sui, L. Zhang, H. Zhou, Q. Chen, *Nat. Commun.* **2019**, *10*, 815.

[27] L. Wang, H. Zhou, J. Hu, B. Huang, M. Sun, B. Dong, G. Zheng, Y. Huang, Y. Chen, L. Li, Z. Xu, N. Li, Z. Liu, Q. Chen, L.-D. Sun, C.-H. Yan, *Science* **2019**, *363*, 265.

[28] E. M. Tennyson, T. A. S. Doherty, S. D. Stranks, *Nat. Rev. Mater.* **2019**, *4*, 573.

[29] C. Stavrakas, A. A. Zhumekenov, R. Brenes, M. Abdi-Jalebi, V. Bulović, O. M. Bakr, E. S. Barnard, S. D. Stranks, *Energy Environ. Sci.* **2018**, *10*, 2846.

[30] T. A. S. Doherty, A. J. Winchester, S. Macpherson, D. N. Johnstone, V. Pareek, E. M. Tennyson, S. Kosar, F. U. Kosasih, M. Anaya, M. Abdi-Jalebi, Z. Andaji-Garmaroudi, E. L. Wong, J. Madéo, Y.-H. Chiang, J.-S. Park, Y.-K. Jung, C. E. Petoukhoff, G. Divitini,

M. K. L. Man, C. Ducati, A. Walsh, P. A. Midgley, K. M. Dani, S. D. Stranks, *Nature* **2020**, *580*, 360.

[31] A. D. Wright, C. Verdi, R. L. Milot, G. E. Eperon, M. A. Pérez-Osorio, H. J. Snaith, F. Giustino, M. B. Johnston, L. M. Herz, *Nat. Commun.* **2016**, *7*, 11755.

[32] Y. Wang, M. I. Dar, L. K. Ono, T. Zhang, M. Kan, Y. Li, L. Zhang, X. Wang, Y. Yang, X. Gao, Y. Qi, M. Grätzel, Y. Zhao, *Science* **2019**, *365*, 591.

[33] K. T. Cho, S. Paek, G. Grancini, C. Roldán-Carmona, P. Gao, Y. Lee, M. K. Nazeeruddin, *Energy Environ. Sci.* **2017**, *10*, 621.